Supporting Information

Effect of Size Selective Retention on the Cotransport of Hydroxyapatite and Goethite Nanoparticles in Saturated Porous Media

Dengjun Wang,[†] Yan Jin,* and Deb P. Jaisi*

Department of Plant and Soil Sciences, University of Delaware, Newark, DE 19716

*Corresponding Authors

Prof. Dr. Yan Jin

E-mail: yjin@udel.edu; Tel.: (302)-831-6962; Fax: (302)-831-0605

Prof. Dr. Deb P. Jaisi

E-mail: jaisi@udel.edu; Tel.: (302)-831-1376; Fax: (302)-831-0605

30 Pages, 1 Table, and 14 Figures

[†] First Author: E-mail: wangdengjun1986@gmail.com (D. Wang).

Table of Contents	**Pages**
S1. Characterizations of hydroxyapatite nanoparticles (HANPs) and goethite nanoparticles (GNPs)	S1−S2
S2. Preparation of Suwannee River humic acid and fulvic acid stock solutions	S2
S3. Determination of the concentration of GNPs stock suspension	S2−S3
S4. Extended Derjaguin-Landau-Verwey-Overbeek (XDLVO) theory	S3−S6
S5. Dissolution of HANPs as a function of pH without/with GNPs copresent in the suspension	S6−S7
S6. Transport model	S7−S8
Table S1. Electrokinetic properties of HANPs-GNPs influents and quarts sands, and DLVO/XDLVO parameters for particle-sand interactions	S9
Fig. S1. SEM images of cleaned quartz sands	S10
Fig. S2. UV-vis absorption spectra and calibration curves of GNPs suspensions	S11
Fig. S3. Powder XRD patterns of HANPs and GNPs	S12
Fig. S4. TEM images and selected-area electron diffraction pattern of GNPs	S13
Fig. S5. FTIR spectra of HANPs and GNPs	S14
Fig. S6. Electrophoretic mobilities of HANPs and GNPs suspensions	S15
Fig. S7. DLVO/XDLVO interaction energies between particle-sand systems	S16
Fig. S8. Dissolution of HANPs as a function of pH	S17
Fig. S9. FTIR spectrum of HANPs-GNPs mixture	S18
Fig. S10. Breakthrough curves of HANPs (or GNPs) without/with GNPs (or HANPs) copresent in the suspension at pH 10.5	S19
Fig. S11. Breakthrough curves of HANPs (or GNPs) without/with HANPs (or GNPs) copresent in the suspension at pH 7.5	S20
Fig. S12. SEM image of quartz sand in column inlet at pH 7.5	S21−S22
Fig. S13. Breakthrough curves of HANPs (or GNPs) under 10 mg L^{-1} SRHA without/with pretreatment of the column with 10 mg L^{-1} SRHA	S23
Fig. S14. TEM images of HANPs-GNPs samples in the effluents under SRHA concentration of 10 mg L^{-1}	S24
References	S25−S28

S1. Characterizations of Hydroxyapatite Nanoparticles (HANPs) and Goethite Nanoparticles (GNPs)

Multiple instruments including X-ray diffractometer, transmission electron microscope (TEM), surface area and porosity analyzer, Fourier transform infrared (FTIR) spectrometer, and electrophoretic mobility (EM) analyzer were employed in this study to characterize the physicochemical properties of the HANPs and GNPs.

Mineral phase identification of the HANPs and GNPs was performed on the Bruker D8 Advance X-ray diffractometer (Bruker Corp., Billerica, MA) using a graphite monochrometer with a Cu Kα source (λ = 1.5406 Å) from 10° to 70° at a step size of 0.02° and a scanning rate of 1° min^{-1}.

The primary size and shape of the GNPs were observed using the JEM-3100 TEM (JEOL; Japan). For TEM imaging, one drop of the GNPs suspension (100 mg L^{-1} and pH 7.5) was placed on a 100 mesh carbon-coated copper grid and then left to air drying. The images were taken at an acceleration voltage of 300 kV.

Specific surface area (SSA) of the GNPs was determined using the Micromeritics 3000 Surface Area and Porosity Analyzer (Micromeritics Instrument Corp., Norcross, GA) based upon the Brunauer-Emmett-Teller (BET) method. For SSA measurement freeze-dried GNPs sample was weighted into a sample cell and outgassed under vacuum (10^{-3} mbar) at 298 K for 24 h.

The function groups of HANPs and GNPs were analyzed using the Thermo Nico FTIR spectrometer equipped with a MCT detector. Spectral analysis was performed using the OMNIC spectroscopy software suite (Thermo Scientific, Waltham, MA).

The HANPs are expected to dissolve at acidic pH conditions,[1] thus the EMs of HANPs were investigated over a narrow pH range. Briefly, the pH of HANPs suspensions (200 mg L^{-1}

and background electrolyte solution of 0.01 M KNO_3) was adjusted using 1 mM HNO_3 or NaOH to achieve pH values ranging from 6.5−11. The EMs of the resulting HANPs suspensions at the desired pHs were measured using the Zetasizer Nano ZS (Malvern Instruments, Southborough, MA). The EMs of GNPs suspensions (100 mg L^{-1} and background electrolyte solution of 0.01 M KNO_3) were determined using the same procedure and protocol but over a wide pH range, i.e., pH = 2.5−11.

S2. Preparation of Suwannee River Humic Acid and Fulvic Acid Stock Solutions

Standard Suwannee River humic acid (SRHA, Standard II, Catalog No.: 2S101H) and fulvic acid (SRFA, Standard I, Catalog No.: 1S101F) were purchased from the International Humic Substances Society (IHSS, St. Paul, MN). Their physicochemical properties such as elemental composition, molecular weight, density, carboxylic acidity, and hydrophobicity have been described by Schlautman and Morgan.[2] Stock solution of the SRHA (or SRFA) was prepared by introducing 100 mg of the SRHA (or SRFA) dry powders in 250 mL of deionized water and stirring the solution overnight. The solution was then filtered through a 0.2 μm cellulose acetate membrane (Thermo Scientific). Total organic carbon (TOC) contents of the SRHA and SRFA stock solutions were determined to be 140 and 148 mg L^{-1}, respectively, using the TOC analyzer (Model Vario TOC Cube, Elementar Americas Inc., Mount Laurel, NJ).

S3. Determination of the Concentration of GNPs Stock Suspension

The concentration of GNPs stock suspension was determined using the UV-vis spectrophotometer (DU Series 640, Beckman Instruments Inc., Fullerton, CA) at the wavelength of 390 nm (Fig. S2a). A calibration curve was constructed by diluting a 200 mg L^{-1} GNPs

suspension (dispersing 0.200 g of GNPs dry powders in 1 L of deionized water and without further treatment, i.e., centrifugation) over the range of 0−200 mg L^{-1}. The calibration curve displayed a high linearity (Fig. S2b).

The UV-vis absorption spectra of the GNPs suspensions without/with 200 mg L^{-1} HANPs are shown in Fig. S2a. The peak wavelengths of GNPs suspensions without/with HANPs were identical (390 nm). Most notably, the absorbance values of GNPs suspensions without/with HANPs at the wavelength of 390 nm were almost the same. These observations indicate that in the concurrent presence of GNPs and HANPs, the concentration of GNPs can be determined spectrophotometrically at the wavelength of 390 nm. A similar finding was recently reported by Cai et al.[3] in their investigation on the cotransport of titanium dioxide and fullerene NPs in water-saturated quartz sand columns.

S4. Extended Derjaguin-Landau-Verwey-Overbeek (XDLVO) Theory

To qualitatively understand the cotransport and retention trends of HANPs and GNPs in water-saturated sand columns at varying pHs, the classical Derjaguin-Landau-Verwey-Overbeek (DLVO)[4, 5] theory was applied to calculate the total particle-sand interaction energy as the sum of Lifshitz-van der Waals (LW) and electrical double layer (EDL) interactions, whereas the extended DLVO (XDLVO) theory that includes the steric interaction was chosen to determine the total interaction energy in the presence of natural organic matter (NOM), i.e., SRHA and SRFA. In this study, the HANPs-GNPs complex is assumed to be uniform sphere, small relative to the sand grain, i.e., a sphere-plate configuration is employed. Ionic strength for the interaction energy calculation is 0.1 mM KNO_3. The expression for the LW interaction energy (Φ_{LW}) is given as follows:[6, 7]

$$\Phi_{\mathrm{LW}} = -\frac{A_{132} d_{\mathrm{p}}}{12h}\left[1 + \frac{14h}{\lambda}\right]^{-1} \quad [1]$$

Where d_{p} is the diameter of the HANPs-GNPs complex, which was taken from the values determined by the dynamic light scattering (DLS); h is the separation distance between particle and collector surface; λ is the characteristic wavelength of interaction, usually taken to be 100 nm;[7] and A_{132} is the combined Hamaker constant for the particle-water-sand system, which can be calculated from the Hamaker constant of individual material using the following equation:[8, 9]

$$A_{132} = \left(\sqrt{A_{11}} - \sqrt{A_{33}}\right)\left(\sqrt{A_{22}} - \sqrt{A_{33}}\right) \quad [2]$$

Where A_{11} is the Hamaker constant for hydroxyapatite (6.00×10^{-20} J)[10] or goethite (5.00×10^{-20} J)[11]. Since the Hamaker constant for hydroxyapatite is greater than that of goethite, the value of 6.00×10^{-20} J is employed. Sorption and (or) coating of NOM onto HANPs and (or) GNPs would occur when NOM is present in the HANPs-GNPs suspensions particularly at high NOM concentrations, thus the Hamaker constant for humic acid (4.85×10^{-20} J)[12] is employed to represent the Hamaker constant for HANPs-GNPs complex in the presence of NOM. A_{22} is the Hamaker constant for quartz sand (8.86×10^{-20} J);[13] and A_{33} is the Hamaker constant for water (3.70×10^{-20} J).[8] The results from Eq. [2] for the combined Hamaker constants for HANPs-GNPs-water-sand and NOM-coated HANPs-GNPs-water-sand systems are 5.54×10^{-21} and 2.94×10^{-21} J, respectively.

The expression for the EDL interaction energy (Φ_{EDL}) is given as:[6, 14]

$$\Phi_{\mathrm{EDL}} = 0.5\pi\varepsilon_0\varepsilon_{\mathrm{r}} d_{\mathrm{p}}\left\{2\psi_{\mathrm{p}}\psi_{\mathrm{c}} \ln\left[\frac{1+\exp(-\kappa h)}{1-\exp(-\kappa h)}\right] + \left(\psi_{\mathrm{p}}{}^2 + \psi_{\mathrm{c}}{}^2\right)\ln[1-\exp(-2\kappa h)]\right\} \quad [3]$$

$$\kappa = \sqrt{\frac{1000 e^2 \sum n_{\mathrm{j0}} z_{\mathrm{j}}^2}{\varepsilon_0 \varepsilon_{\mathrm{r}} kT}} \quad [4]$$

Where ε_0 and ε_{r} are the dielectric permittivity of vacuum (8.854×10^{-12} C V^{-1} m^{-1}) and water (78.5), respectively; ψ_{p} and ψ_{c} are the zeta (ζ) potentials of particle (HANPs-GNPs

complex) and collector (quartz sand), respectively; κ is the Debye-Hückel parameter; e is the charge of an electron (1.602×10^{-19} C); n_{j0} is the number concentration of ions in the bulk suspension (6.022×10^{19} L^{-1}); z_j is the ion valence (1); k is the Boltzmann constant (1.38×10^{-23} J K^{-1}); and T is the absolute temperature (298 K).

In the presence of NOM, two additional repulsive interactions should be considered: osmotic repulsion (Φ_{OSM}) and elastic-steric repulsion (Φ_{ELAS}) interaction energies.[15] Overlap of the NOM layer on two approaching particles increases the local NOM segment concentration and thus enhances the local osmotic pressure in the overlap region (Φ_{OSM}). The expression for Φ_{OSM} is given as follows:[15]

$$\frac{\Phi_{OSM}}{kT} = 0 \qquad 2d \le h$$

$$\frac{\Phi_{OSM}}{kT} = \frac{2\pi d_p}{v_1}\phi_{NOM}^2\left(\frac{1}{2}-\chi\right)\left(d-\frac{h}{2}\right)^2 \qquad d \le h < 2d$$

$$\frac{\Phi_{OSM}}{kT} = \frac{2\pi d_p}{v_1}\phi_{NOM}^2\left(\frac{1}{2}-\chi\right)\left(\frac{h}{2d}-\frac{1}{4}-\ln\left(\frac{h}{d}\right)\right) \qquad h < d \qquad [5]$$

Where v_1 is the volume of a solvent molecule (0.03 nm^3);[16] χ is the Flory-Huggins solvency parameter (0.45);[16] d is the thickness of sorbed NOM molecule (i.e., 2.25 and 1.49 nm for the SRHA and SRFA, respectively);[2] and ϕ_{NOM} is the density (or effective volume fraction) of the sorbed NOM layer, which was assumed to be 5.0×10^{-3}, 1.0×10^{-2}, and 1.5×10^{-2} when SRHA (or SRFA) concentration was 0.1, 1, and 10 mg L^{-1}, respectively.[16]

Any compression of the sorbed NOM layer below the thickness of the unperturbed layer (d) leads to a loss of entropy and gives rise to the elastic-steric repulsion (Φ_{ELAS}).[15]

$$\frac{\Phi_{ELAS}}{kT} = 0 \qquad d \le h$$

$$\frac{\Phi_{ELAS}}{kT} = \frac{\pi d_p}{M_w}\phi_{NOM} d^2 \rho_{NOM}\left(\frac{h}{d}\ln\left(\frac{h}{d}\left(\frac{3-\frac{h}{d}}{2}\right)^2\right) - 6\ln\left(\frac{3-\frac{h}{d}}{2}\right) + 3(1+\frac{h}{d})^2\right) \qquad d > h \qquad [6]$$

Where M_W is the molecular weight of NOM (i.e., 3357 and 2114 Da for the SRHA and SRFA, respectively)[17] and ρ_{NOM} is the density of NOM (i.e., 1.508 and 1.427 g cm^{-3} for the SRHA and SRFA, respectively).[2]

To summarize, the total DLVO interaction energy ($\Phi_{TOT\text{-}DLVO}$) for the particle-water-sand system at varying pHs is:

$$\Phi_{TOT-DLVO} = \Phi_{LW} + \Phi_{EDL} \quad [7]$$

And the total XDLVO interaction energy ($\Phi_{TOT\text{-}XDLVO}$) in the presence of NOM is:

$$\Phi_{TOT-XDLVO} = \Phi_{LW} + \Phi_{EDL} + \Phi_{OSM} + \Phi_{ELAS} \quad [8]$$

It is important to emphasize that the DLVO/XDLVO theory described above is based upon a number of assumptions. For example, the DLVO/XDLVO calculations employ average ζ potentials and assume geometrically smooth (physically) and chemically homogeneous surfaces for colloids and collectors. In this work, however, the HANPs, GNPs, and HANPs-GNPs complexes are not spherical in shape and the quartz sands utilized also exhibit some degree of physical heterogeneity, e.g., surface roughness as shown in Fig. S1. Furthermore, the HANPs are expected to dissolve at low pH that will likely influence their surface charge distribution and ζ potential. Therefore, the above DLVO/XDLVO calculations should be only viewed as a first approximation of anticipated changes in mean interaction energy in response to variability in pH and NOM concentration and type.

S5. Dissolution of HANPs as a Function of pH Without/With GNPs Copresent in the Suspension

The PO_4^{3-} ion released from HANPs without/with GNPs copresent in the suspensions was monitored at varying pHs over the time frame of the cotransport experiments (~1.1 h). Batch

experiments were conducted in triplicate (n = 3) in 15 mL centrifuge tubes. The pH of HANPs and HANPs-GNPs suspensions (HANPs, GNPs, and KNO_3 concentrations were 200 mg L^{-1}, 100 mg L^{-1}, and 0.1 mM, respectively) was adjusted using 1 mM HNO_3 or NaOH to obtain pH values of 6.5, 7.5, 8.5, 9.5, and 10.5, respectively. Subsequently, the resulting suspension was gently shaken at a speed of 30 rpm[18] for 1.1 h. The sample was centrifuged at 15,000g for 1 h and the supernatant was then ultrafiltered using a 10 kDa regenerated cellulose membrane[18, 19] (No.: PLGC02510, EMD Millipore Corp., Billerica, MA) with a nominal particle size limit of 11.3 nm[20] to remove HANPs and (or) HANPs-GNPs complexes from the suspension. The concentration of PO_4^{3-} ion in the filtrate was quantified using the phosphomolybdate method.[21] Here the dissolved PO_4^{3-} ion refers to the P species that pass through a 10 kDa regenerated cellulose membrane, considering that the HANPs and (or) HANPs-GNPs complexes cannot pass through the membrane.

S6. Transport Model

A one-dimensional form of the advection-dispersion equation (ADE) with one kinetic retention site was used to simulate the transport and retention of HANPs and GNPs, respectively, at varying pHs and SRHA and SRFA concentrations as follows:[22]

$$\frac{\partial(\theta_w C)}{\partial t} = \frac{\partial}{\partial z}\left(\theta_w D \frac{\partial C}{\partial z}\right) - \frac{\partial(qC)}{\partial z} - \theta_w \psi k_r C \quad [9]$$

$$\frac{\partial(\rho_b S)}{\partial t} = \theta_w \psi k_r C \quad [10]$$

Where θ_w is the volumetric water content [−], C is the HANPs (or GNPs) concentration in the aqueous phase [M L^{-3}, M and L denote units of mass and length, respectively], t is time [T, T denotes time unit], z is the distance from column inlet [L], D is the hydrodynamic dispersion coefficient [L^2 T^{-1}], q is the Darcy water flux [L T^{-1}], ψ is a dimensionless function to account

for both time- and depth-dependent blocking [−], k_r is the first-order retention rate coefficient of HANPs (or GNPs) from aqueous to solid phase, ρ_b is the bulk density of porous medium [M L^{-3}], and S is the solid-phase concentration of retained HANPs (or GNPs) [M M^{-1}]. The expression for the blocking term (ψ) is given as:[23]

$$\psi = \left(1 - \frac{S}{S_{max}}\right)\left(\frac{d_{50}+z}{d_{50}}\right)^{-\beta} \quad [11]$$

Where d_{50} is the median grain size of porous medium [L], β is an empirical parameter controlling the shape of spatial distribution for retained HANPs (or GNPs) [−],[24] and S_{max} is the maximum solid-phase concentration of retained HANPs (or GNPs) [M M^{-1}]. The first term on the right hand side of Eq. [11] accounts for filling of retention sites in a manner similar to the Langmuirian blocking approach,[25] whereas the second term on the right hand site describes depth-dependent retention.[24]

Transport model parameters of S_{max}/C_o (normalized maximum solid-phase concentration of retained particles), k_r, and β were obtained from the observed breakthrough curves (BTCs) and retention profiles (RPs) of HANPs (or GNPs) using a nonlinear least squares optimization routine coded in HYDRUS-1D.[22] It should be mentioned that at different pHs, the shapes of RPs for both HANPs and GNPs were hyperexponential, i.e., a decreasing rate of retention with depth. It is noted that β = 0.432 can well capture the hyperexponential RPs of both colloids[24] and NPs.[26] Consequently, β = 0.432 was employed for model simulation at different pH tests to minimize the number of model-fitted parameters.

Table S1. Electrokinetic Properties of HANPs-GNPs Influents and Quartz Sands, and DLVO/XDLVO Parameters for the Particle-Sand Interactions Under Different pHs and NOM Concentrations and Types

pH	SRHA (mg L^{-1})	SRFA (mg L^{-1})	HANPs-GNPs influent		Quartz sand		Φ_{max} (kT)
			EM (10^{-8} m^2 s^{-1} V^{-1})	ζ potential (mV)	EM (10^{-8} m^2 s^{-1} V^{-1})	ζ potential (mV)	
6.5			–0.10 ± 0.02 a	–1.27 ± 0.20 a	–1.62 ± 0.09 a	–20.7 ± 1.2 a	<0
7.5			–0.21 ± 0.03 a	–2.65 ± 0.34 a	–1.62 ± 0.10 a	–21.3 ± 1.4 a	<0
10.5			–1.52 ± 0.13 b	–19.4 ± 1.59 b	–3.42 ± 0.09 b	–43.6 ± 1.2 b	127
7.6	0.1		–1.06 ± 0.07 b	–13.6 ± 0.91 b	–1.66 ± 0.21 a	–21.1 ± 2.7 a	149
7.6	1		–1.37 ± 0.07 c	–17.6 ± 0.83 c	–1.98 ± 0.17 b	–25.3 ± 2.1 b	209
7.6	10		–1.66 ± 0.08 d	–21.1 ± 1.03 d	–3.12 ± 0.23 c	–39.8 ± 2.9 c	297
7.7		0.1	–0.70 ± 0.07 b	–8.96 ± 0.89 b	–1.81 ± 0.19 a	–23.1 ± 2.5 a	78.6
7.7		1	–1.23 ± 0.07 c	–15.7 ± 0.94 c	–1.85 ± 0.15 a	–24.0 ± 2.2 a	152
7.7		10	–1.70 ± 0.06 d	–21.7 ± 0.75 d	–2.63 ± 0.17 b	–33.6 ± 2.2 b	229

EM, Electrophoretic mobility; ζ potential, Zeta potential; Φ_{max}, Energy barrier to the primary minimum as calculated by DLVO/XDLVO theory; Mean values ± standard deviations are given for EMs and ζ potentials; Mean values in each vertical column followed by the same lowercase letters are not significantly different using Tukey's honestly significant difference (HSD) test at $p < 0.05$.

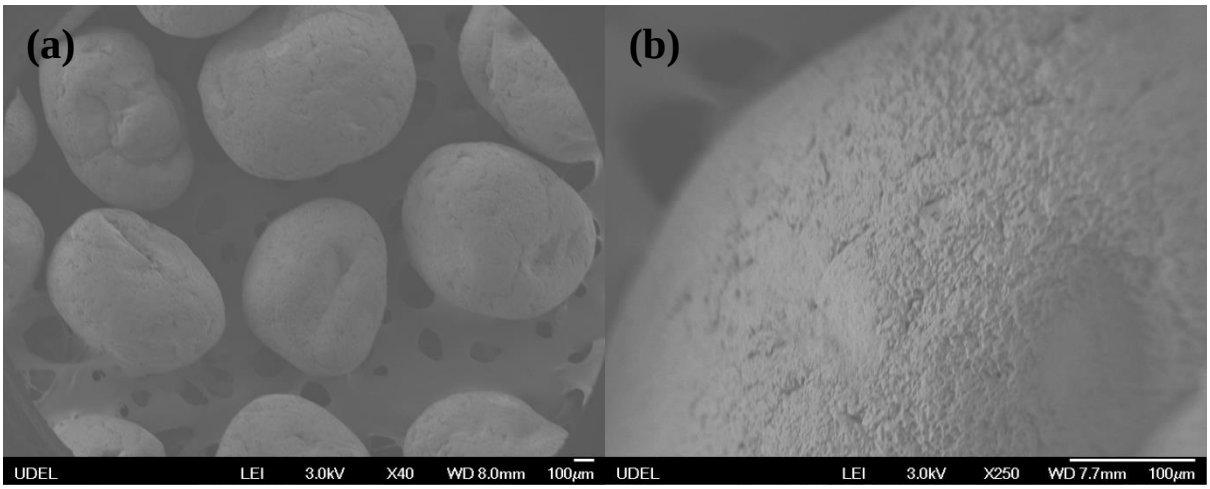

Fig. S1. Scanning electron microscope (SEM) images of cleaned quartz sands. The quartz sands are roughly spherical in shape and exhibit some degrees of physical heterogeneity, e.g., surface roughness.

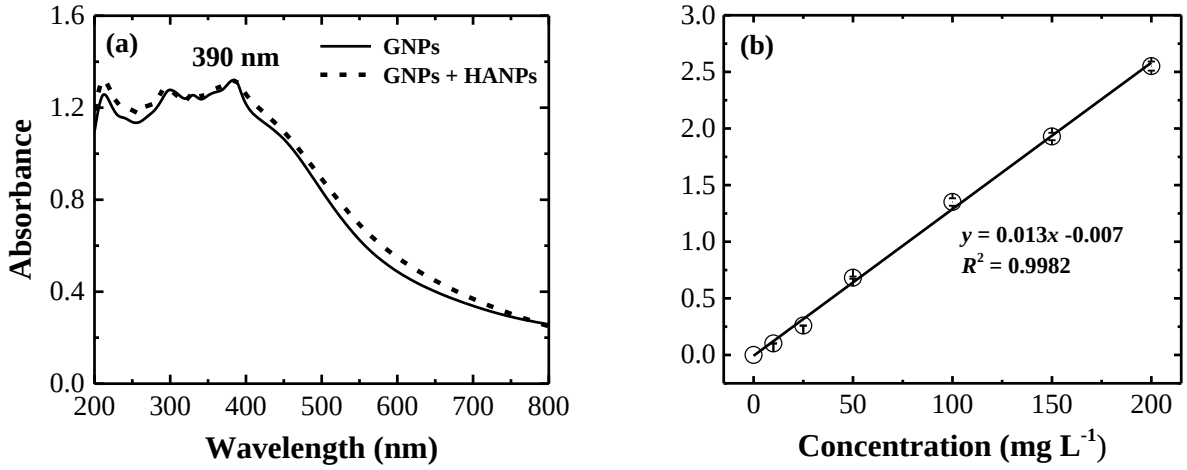

Fig. S2. (a) UV-vis absorption spectra of GNPs suspensions at 100 mg L^{-1} and pH 7.5 without (solid line) and with 200 mg L^{-1} HANPs (dotted line) copresent in the suspensions. (b) Calibration curve of the GNPs suspension (without centrifugation) within the concentration range of 0−200 mg L^{-1} (pH 7.5) at the wavelength of 390 nm. Error bars represent the standard deviations (n = 3).

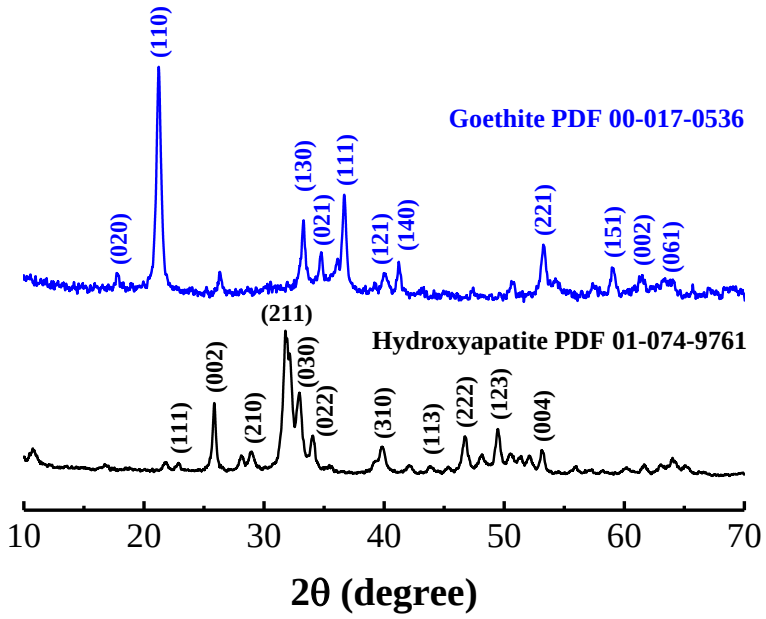

Fig. S3. Powder X-ray diffraction patterns of HANPs (black solid line) and GNPs (blue solid line). The HANPs and GNPs were found to be single phase pure hydroxyapatite (PDF 01-074-9761) and goethite (PDF 00-017-0536) minerals, respectively, based on the Joint Committee on Powder Diffraction Standards and no characteristic peak of impurity was encountered.

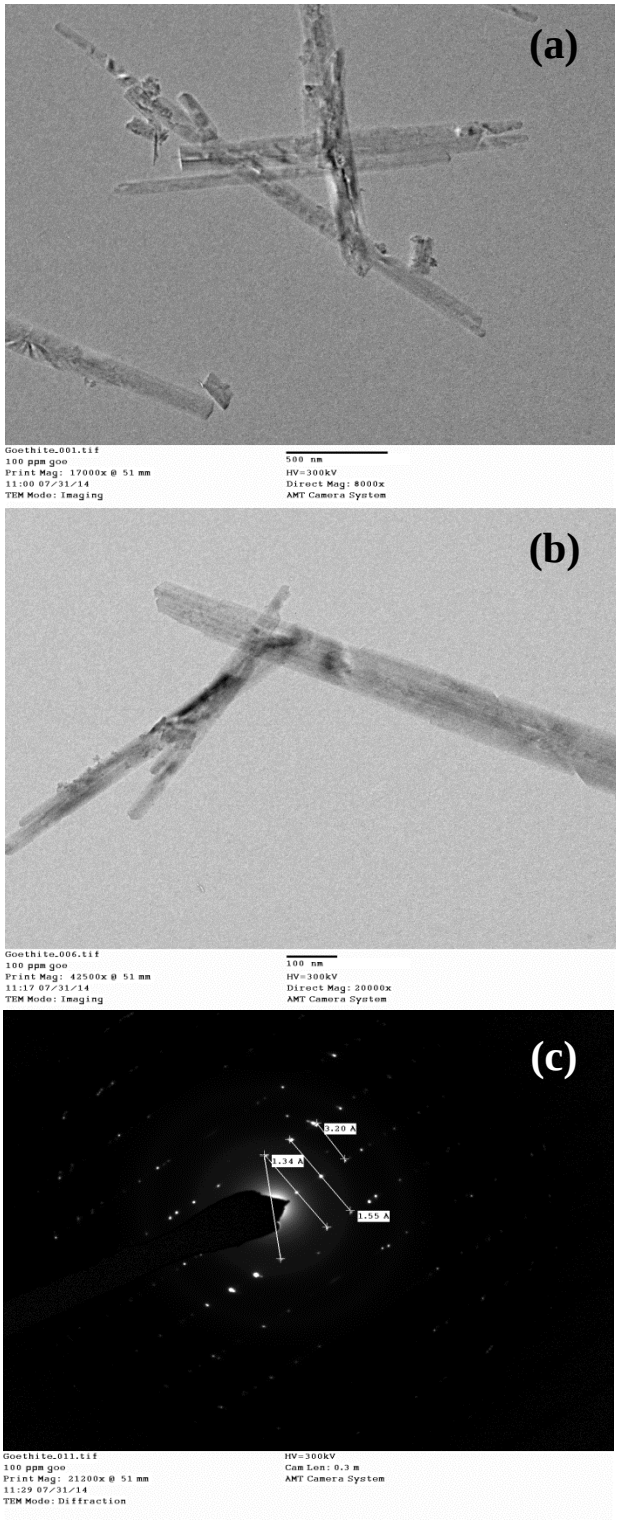

Fig. S4. TEM images (a, b) and corresponding selected-area electron diffraction pattern (c) of the GNPs suspension at 100 mg L^{-1} and pH 7.5. Scale bars in (a, b) are 500 and 100 nm, respectively. The GNPs are acicular crystals that are 90 nm wide and 1850 nm long using TEM counting technique (Image J software).

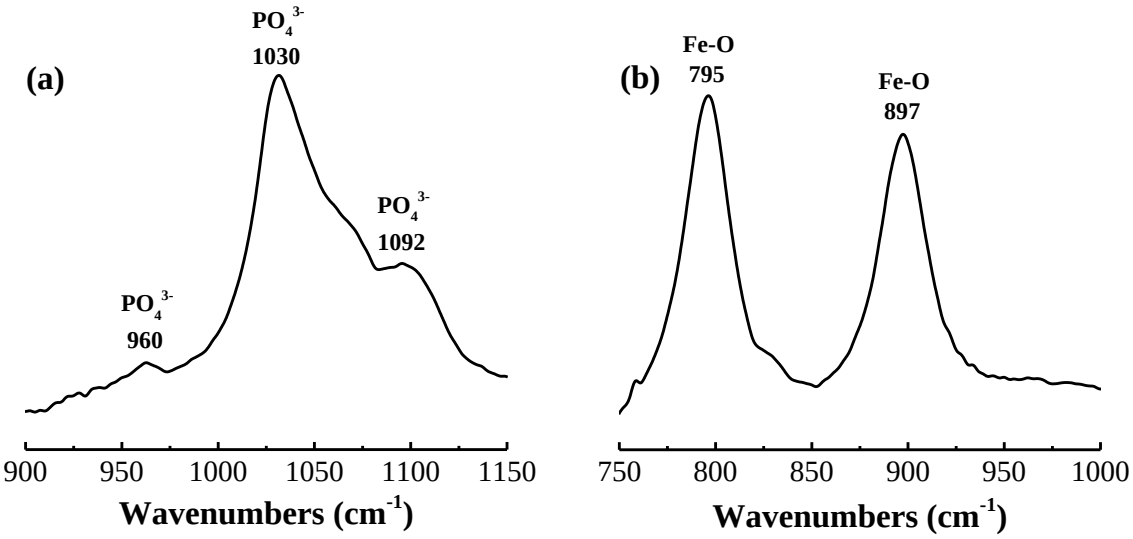

Fig. S5. FTIR spectra of the HANPs (a) and GNPs (b). For HANPs, the three characteristic bands at 960, 1030, and 1092 cm^{-1} are assigned to PO_4^{3-} stretching vibrations,[27, 28] whereas the two characteristic peaks at 795 and 897 cm^{-1} are attributed to Fe-O stretching vibrations for GNPs[29, 30].

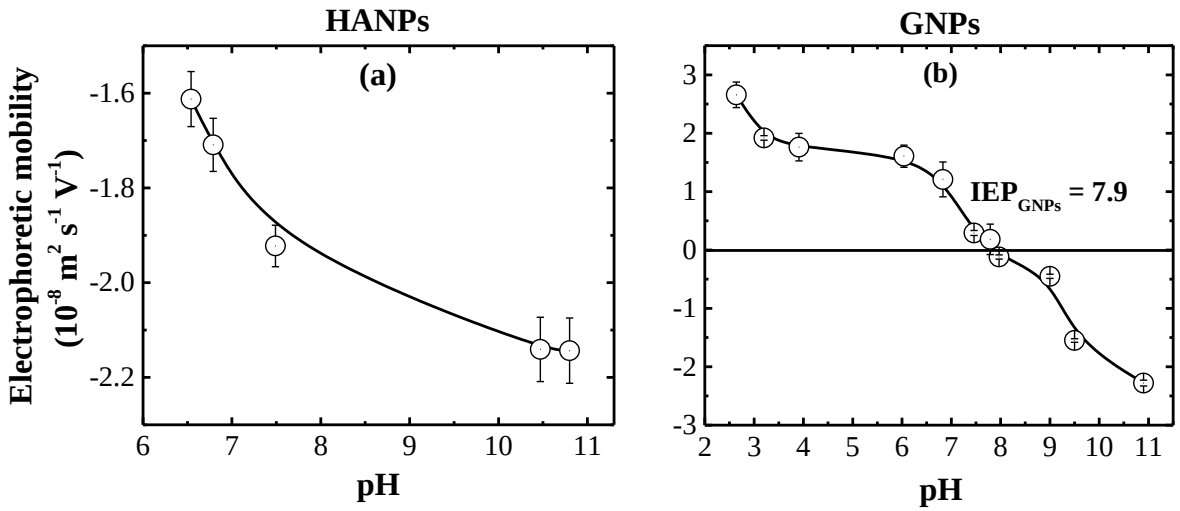

Fig. S6. Electrophoretic mobilities of HANPs (a) and GNPs (b) suspensions as a function of pH under 0.01 M KNO_3. Error bars represent the standard deviations. The HANPs were found to be negatively charged over the range of pH investigated. The EMs of HANPs increased (more negative) from –1.61 to –2.14 × 10^{-8} m^2 s^{-1} V^{-1} when suspension pH was increased from 6.5 to 10.8 (a). The isoelectric point of GNPs (IEP_{GNPs}) was determined to be around pH 7.9 (b), which is in close agreement with previously reported values (pH = 7.6–9.4).[31]

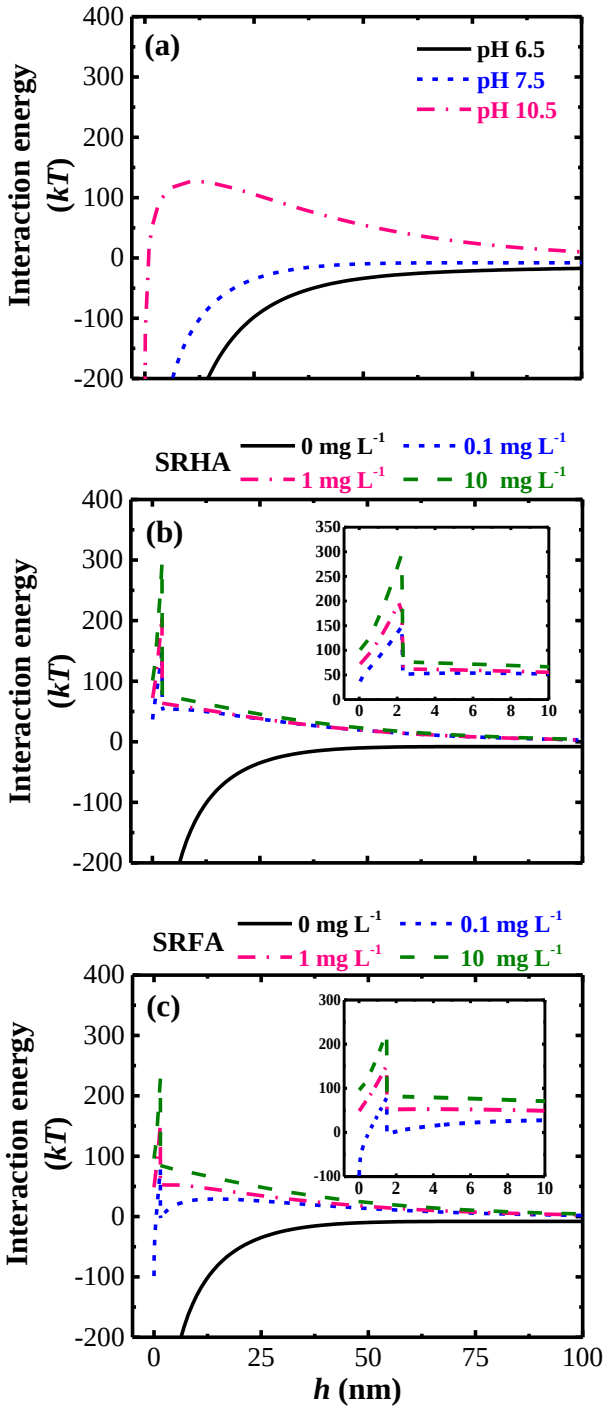

Fig. S7. Calculated DLVO/XDLVO interaction energies plotted as a function of separation distance (*h*) at varying pHs (a) and SRHA (b) and SRFA (c) concentrations. Insets in (b, c) highlight the primary energy barrier (Φ_{max}).

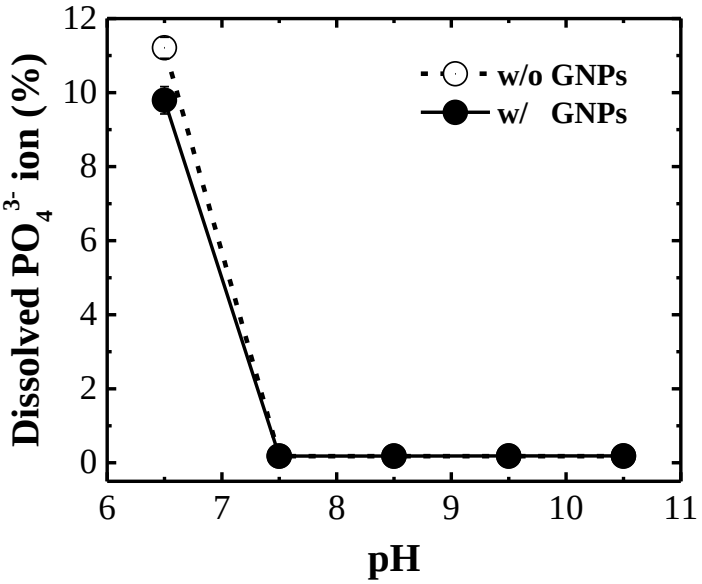

Fig. S8. Dissolution of HANPs as a function of pH without/with GNPs copresent in the suspensions over the time frame of the cotransport experiments (~1.1 h) in batch experiments. The concentrations of HANPs and GNPs in the suspensions were 200 and 100 mg L^{-1}, respectively. The line is just connection between data points. Dissolved PO_4^{3-} ion in % was calculated as $[PO_4^{3-}]/[P]_{total} \times 100\%$. The error bars represent the standard deviations (n = 3).

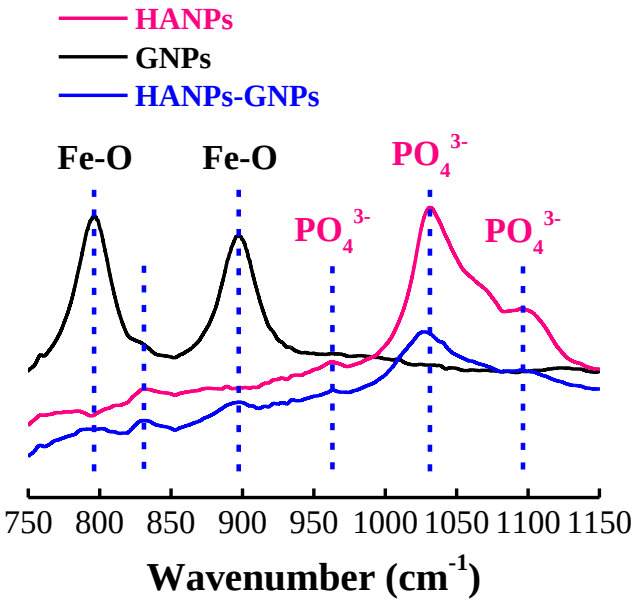

Fig. S9. FTIR spectra of the HANPs (pink solid line), GNPs (black solid line), and HANPs-GNPs mixture (blue solid line). The HANPs-GNPs mixture was generated by freeze-drying the solid sample in batch experiments at pH 7.5 (see S5 for details). The copresence of PO_4^{3-} and Fe-O characteristic bands indicates that the mixture is the HANPs-GNPs complex.

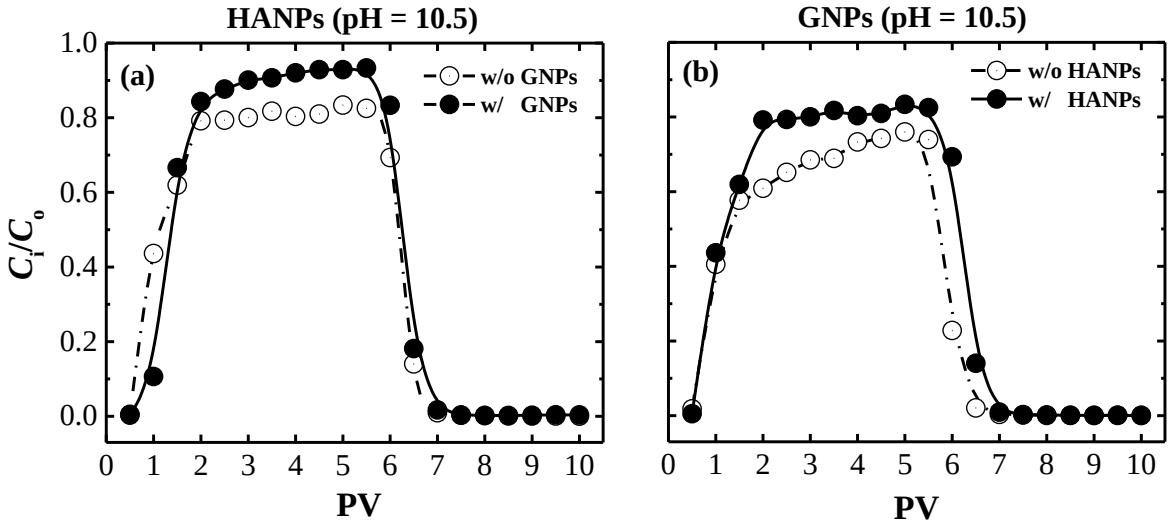

Fig. S10. (a) Breakthrough curves of HANPs without (open symbol) and with (solid symbol) GNPs copresent in suspensions at pH 10.5 in saturated sand columns when d_{50} = 688 μm and Darcy velocity of 0.441 cm min^{-1}. (b) Similar information for the GNPs without and with HANPs copresent in suspensions. The concentrations of HANPs and GNPs in the suspensions were 200 and 100 mg L^{-1}, respectively. The lines in (a, b) are just connection between data points. For HANPs (a), total effluent recoveries (M_{eff}) were 83.9 and 90.6%, respectively, without and with GNPs copresent in suspensions, whereas the M_{eff} values of GNPs (b) were 68.7 and 83.7%, respectively, without and with HANPs copresent in suspensions. It is evident that the mobility of HANPs (or GNPs) individually was less than that of HANPs (or GNPs) in the copresence of GNPs (or HANPs).

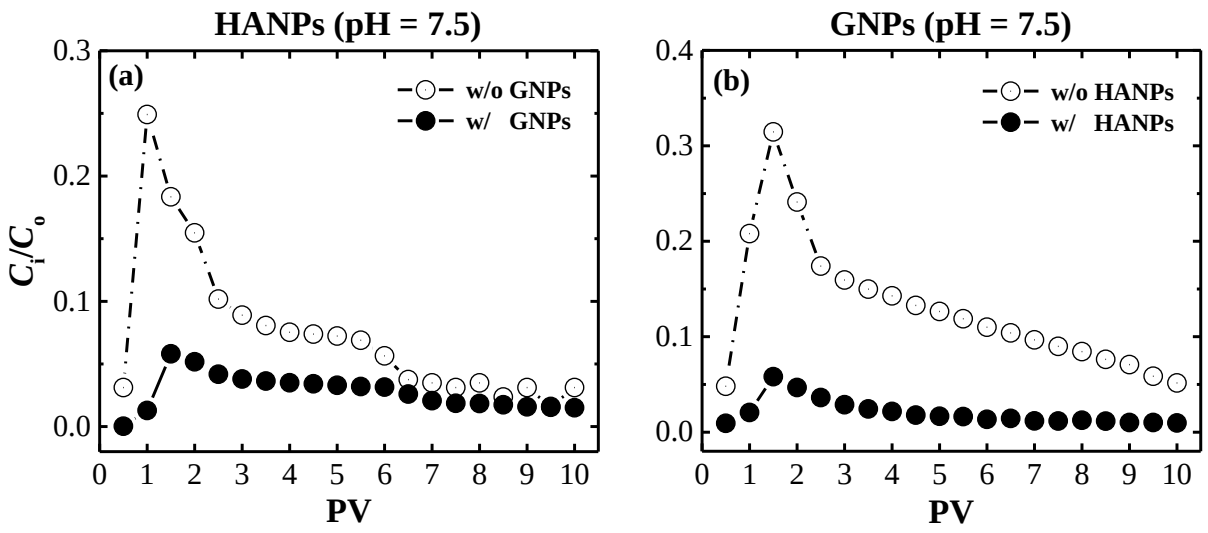

Fig. S11. (a) Breakthrough curves of HANPs without (open symbol) and with (solid symbol) GNPs copresent in suspensions at pH 7.5 in saturated sand columns when d_{50} = 688 μm and Darcy velocity of 0.441 cm min^{-1}. (b) Similar information for the GNPs without and with HANPs copresent in suspensions. The concentrations of HANPs and GNPs in the suspensions were 200 and 100 mg L^{-1}, respectively. The lines in (a, b) are just connection between data points. For HANPs (a), total effluent recoveries (M_{eff}) were 14.8 and 5.52%, respectively, without and with GNPs copresent in suspensions, whereas the M_{eff} values of GNPs (b) were 25.6 and 4.02%, respectively, without and with HANPs copresent in suspensions. The average hydrodynamic diameter of individual HANPs (907 nm) or GNPs (626 nm) suspension was much smaller than the one of the HANPs-GNPs mixed influent (1656 nm), suggesting that the influent particle size is an indicator of mobility for NPs with larger particles having lower mobility due to greater degrees of interception and sedimentation during transport in porous media.

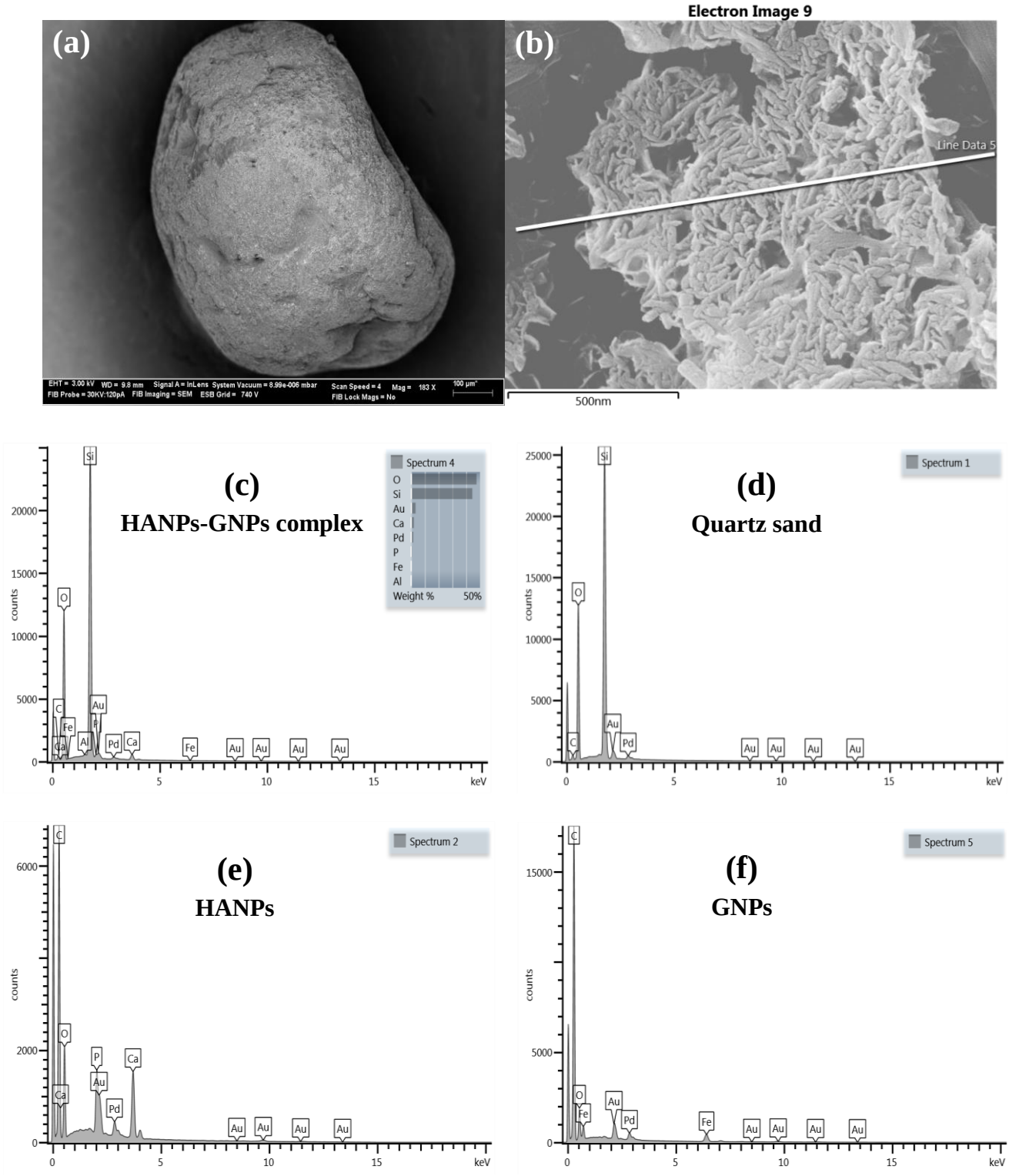

Fig. S12. (a) SEM image of the quartz sand excavated from the column inlet (0−1 cm) after completion of the cotransport experiment of HANPs and GNPs at pH 7.5 in saturated sand

columns when d_{50} = 688 μm and Darcy velocity of 0.441 cm min^{-1}. (b) A higher magnification of the excavated quartz sand. (c) The corresponding energy-dispersive X-ray spectrum of the retained HANPs-GNPs complexes on the quartz sand based upon the line scanning technique. (d), (e), and (f) The energy-dispersive X-ray spectra of cleaned quartz sand, individual HANPs, and individual GNPs, respectively. The presence of Ca, P, O, and Fe elements (c) were consistent with the basic components of HANPs (e) and GNPs (f). The carbon element is shown in (c−f) because the carrier (tape) for holding the SEM sample contains carbon. Scale bars in (a) and (b) are 100 μm and 500 nm, respectively.

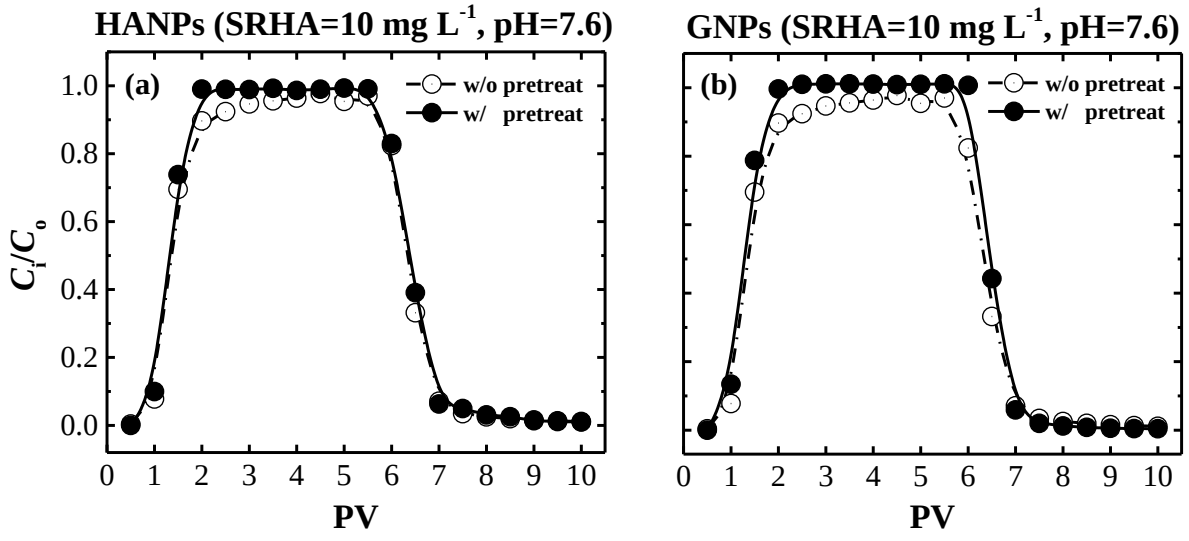

Fig. S13. Breakthrough curves of HANPs (a) and GNPs (b), respectively, without (open symbol) and with (solid symbol) 3 PVs of 10 mg L^{-1} SRHA pretreatment of the column at pH 7.6 and Darcy velocity of 0.441 cm min^{-1} in the presence of 10 mg L^{-1} SRHA. The concentrations of HANPs and GNPs in the suspensions were 200 and 100 mg L^{-1}, respectively. The lines in (a, b) are just connection between data points. In comparing HANPs and GNPs breakthrough curves (BTCs) for the untreated and SRHA-pretreated sand columns, the normalized effluent concentration (C_i/C_o) in the steady-state portion of the NPs BTCs was subject to less variability in the SRHA-pretreated system. These observations imply that there is spatial variability in surface charge on the collector surfaces and that SRHA may even this out. In addition, the M_{eff} values for both HANPs (M_{eff} = 102% > 97.1%) and GNPs (M_{eff} = 106% > 100%) were greater in SRHA-pretreated sands than those without pretreatment with SRHA. Consequently, the SRHA acts to modify the surface charge of the collector by masking some of the positive charge associated with metal oxide impurities. These findings are in good agreement with the results documented in the literature.[3, 32, 33]

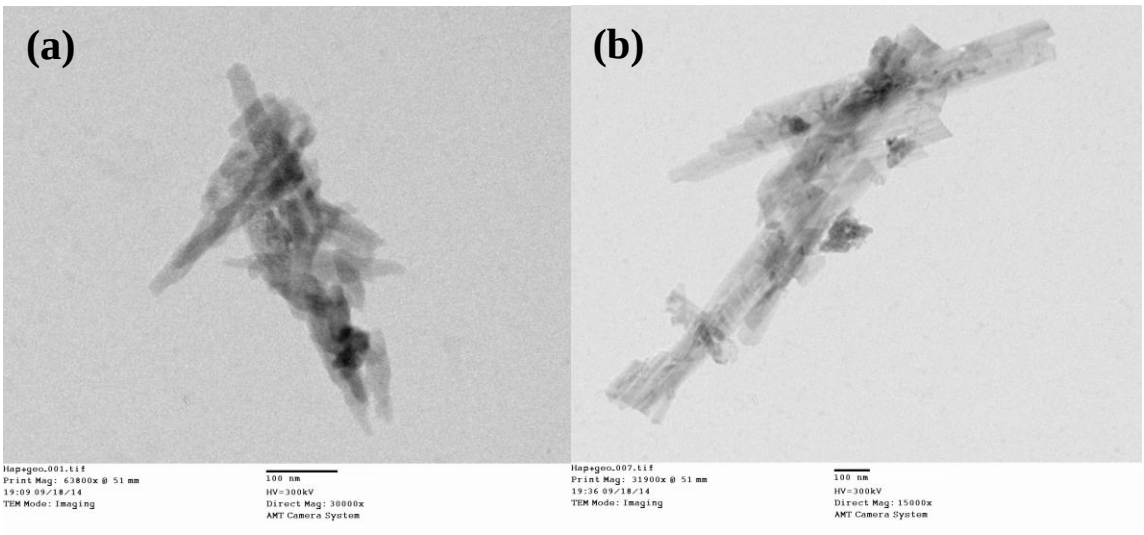

Fig. S14. TEM images of the HANPs aggregates (a) and GNPs aggregates (b) in the effluents when SRHA = 10 mg L^{-1} and pH = 7.6 in saturated sand column when d_{50} = 688 μm and Darcy velocity of 0.441 cm min^{-1}. The scale bar in (a, b) is 100 nm.

REFERENCES

1. Zhang, P.; Ryan, J. A. Formation of pyromorphite in anglesite-hydroxyapatite suspensions under varying pH conditions. *Environ. Sci. Technol.* **1998,** *32* (21), 3318-3324.
2. Schlautman, M. A.; Morgan, J. J. Adsorption of aquatic humic substances on colloidal-size aluminum oxide particles: Influence of solution chemistry. *Geochim. Cosmochim. Acta* **1994,** *58* (20), 4293-4303.
3. Cai, L.; Tong, M. P.; Ma, H.; Kim, H. Cotransport of titanium dioxide and fullerene nanoparticles in saturated porous media. *Environ. Sci. Technol.* **2013,** *47* (11), 5703-5710.
4. Derjaguin, B. V.; Landau, L. D. Theory of the stability of strongly charged lyophobic sols and of the adhesion of strongly charged particles in solutions of electrolytes. *Acta Physicochim. USSR* **1941,** *14*, 633-662.
5. Verwey, E. J. W.; Overbeek, J. T. G. Theory of the Stability of Lyophobic Colloids. Elsevier, Amsterdam, **1948**.
6. Elimelech, M.; Gregory, J.; Jia, X.; Williams, R. Particle Deposition and Aggregation: Measurement, Modelling and Simulation. Butterworth-Heinemann: Woburn, MA, **1995**.
7. Gregory, J. Approximate expressions for retarded van der Waals interaction. *J. Colloid Interface Sci.* **1981,** *83* (1), 138-145.
8. Israelachvili, J. N. Intermolecular and Surface Forces. Academic Press: San Diego, CA, **1992**.
9. Bergendahl, J.; Grasso, D. Prediction of colloid detachment in a model porous media: Thermodynamics. *AIChE J.* **1999,** *45* (3), 475-484.

10. Tian, J.; Zhang, Y.; Guo, X.; Dong, L. Preparation and characterization of hydroxyapatite suspensions for solid freeform fabrication. *Ceram. Int.* **2002,** *28* (3), 299-302.

11. Svoboda, J. A theoretical approach to the magnetic flocculation of weakly magnetic minerals. *Int. J. Miner. Process.* **1981,** *8* (4), 377-390.

12. Hu, J. D.; Zevi, Y.; Kou, X. M.; Xiao, J.; Wang, X. J.; Jin, Y. Effect of dissolved organic matter on the stability of magnetite nanoparticles under different pH and ionic strength conditions. *Sci. Total Environ.* **2010,** *408* (16), 3477-3489.

13. Bergstrom, L. Hamaker constants of inorganic materials. *Adv. Colloid Interface Sci.* **1997,** *70*, 125-169.

14. Hogg, R.; Healy, T. W.; Fuersten, D. W. Mutual coagulation of colloidal dispersions. *T. Faraday Soc.* **1966,** *62*, 1638-1651.

15. Fritz, G.; Schadler, V.; Willenbacher, N.; Wagner, N. J. Electrosteric stabilization of colloidal dispersions. *Langmuir* **2002,** *18* (16), 6381-6390.

16. Phenrat, T.; Saleh, N.; Sirk, K.; Kim, H. J.; Tilton, R. D.; Lowry, G. V. Stabilization of aqueous nanoscale zerovalent iron dispersions by anionic polyelectrolytes: Adsorbed anionic polyelectrolyte layer properties and their effect on aggregation and sedimentation. *J. Nanopart. Res.* **2008,** *10* (5), 795-814.

17. Her, N.; Amy, G.; Foss, D.; Cho, J. Variations of molecular weight estimation by HP-size exclusion chromatography with UVA versus online DOC detection. *Environ. Sci. Technol.* **2002,** *36* (15), 3393-3399.

18. Li, X.; Lenhart, J. J. Aggregation and dissolution of silver nanoparticles in natural surface water. *Environ. Sci. Technol.* **2012,** *46* (10), 5378-5386.

19. Levard, C.; Mitra, S.; Yang, T.; Jew, A. D.; Badireddy, A. R.; Lowry, G. V.; Brown, G. E. Effect of chloride on the dissolution rate of silver nanoparticles and toxicity to *E. coli*. *Environ. Sci. Technol.* **2013,** *47* (11), 5738-5745.

20. Sorensen, T. S. Surface Chemistry and Electrochemistry of Membranes. Marcel Dekker Inc., New York, NY, **1999**.

21. Murphy, J.; Riley, J. P. A modified single solution method for the determination of phosphate in natural waters. *Anal. Chem. Acta* **1962,** *27*, 31-36.

22. Simunek, J.; Sejna, M.; van Genuchten, M. T. The HYDRUS-1D software package for simulating the one-dimensional movement of water, heat, and multiple solutes in variably saturated media, version 4.16. University of California, Riverside, CA, USA, **2008**.

23. Bradford, S. A.; Simunek, J.; Walker, S. L. Transport and straining of *E. coli* O157 : H7 in saturated porous media. *Water Resour. Res.* **2006,** *42* (12).

24. Bradford, S. A.; Simunek, J.; Bettahar, M.; van Genuchten, M. T.; Yates, S. R. Modeling colloid attachment, straining, and exclusion in saturated porous media. *Environ. Sci. Technol.* **2003,** *37* (10), 2242-2250.

25. Adamczyk, Z.; Siwek, B.; Zembala, M.; Belouschek, P. Kinetics of localized adsorption of colloid particles. *Adv. Colloid Interface Sci.* **1994,** *48*, 151-280.

26. Liang, Y.; Bradford, S. A.; Simunek, J.; Vereecken, H.; Klumpp, E. Sensitivity of the transport and retention of stabilized silver nanoparticles to physicochemical factors. *Water Res.* **2013,** *47* (7), 2572-2582.

27. Gibson, I. R.; Best, S. M.; Bonfield, W. Chemical characterization of silicon-substituted hydroxyapatite. *J. Biomed. Mater. Res.* **1999,** *44* (4), 422-428.

28. Panda, R. N.; Hsieh, M. F.; Chung, R. J.; Chin, T. S. FTIR, XRD, SEM and solid state NMR investigations of carbonate-containing hydroxyapatite nano-particles synthesized by hydroxide-gel technique. *J. Phys. Chem. Solids* **2003,** *64* (2), 193-199.

29. Schwertmann, U.; Cornell, R. M. Iron Oxides in the Laboratory: Preparation and Characterization, Second Edition. WILEY-VCH Verlag GmbH, **2000**.

30. Cambier, P. Infrared study of goethites of varying crystallinity and particle size: I. Interpretation of OH and lattice vibration frequencies. *Clay Miner.* **1986,** *21*, 191-200.

31. Kosmulski, M. The pH-dependent surface charging and points of zero charge: V. Update. *J. Colloid Interface Sci.* **2011,** *353* (1), 1-15.

32. Tufenkji, N.; Elimelech, M. Breakdown of colloid filtration theory: Role of the secondary energy minimum and surface charge heterogeneities. *Langmuir* **2005,** *21* (3), 841-852.

33. Wang, D. J.; Bradford, S. A.; Harvey, R. W.; Gao, B.; Cang, L.; Zhou, D. M. Humic acid facilitates the transport of ARS-labeled hydroxyapatite nanoparticles in iron oxyhydroxide-coated sand. *Environ. Sci. Technol.* **2012,** *46* (5), 2738-2745.